Additive manufacturing of fire retardant ethylene-vinyl acetate

*Laura GEOFFROY [1], Fabienne SAMYN [1], Maude JIMENEZ [1], Serge BOURBIGOT [1,]**

[1] Univ. Lille, CNRS UMR 8207, UMET – Unité Matériaux et Transformations, ENSCL, F-59000 Lille, France ;

laura.geoffroy@univ-lille.fr (L.G.), fabienne.samyn@ensc-lille.fr (F.S.), maude.jimenez@univ-lille.fr (M.J.)

* Correspondence: serge.bourbigot@ensc-lille.fr (S.B.); Tel.: +33 (0)3 20 43 48 88

KEYWORDS: Thermocompression, 3D printing, Fused Deposition Modeling, Fire properties

ABSTRACT: Thermocompression (with also extrusion and injection molding) is a classical polymer shaping manufacturing, but it does not easily allow designing sophisticated shapes without using a complex mold, on the contrary to 3D printing (or Polymer Additive manufacturing), which is a very flexible technique. Among all 3D printing techniques, Fused Deposition Modeling is of high potential for product manufacturing, with the capability to compete with conventional polymer processing techniques. This is a quite low cost 3D printing technique, but the range of filaments commercially available is limited. However, in some specific 3D printing processes, no filaments are necessary. Polymers pellets feed directly the printing nozzle allowing to investigate many polymeric matrices with no commercial limitation. This is of high interest for the design of flame retarded materials, but literature is scarce in that field. In this paper, a comparison between thermocompression and 3D printing processes was performed on both neat ethylene-vinyl acetate copolymer (EVA) and EVA flame retarded with Aluminum TriHydroxyde (ATH) containing different loadings (30 or 65 wt%) and with Expandable Graphite (EG), i.e. EVA/ATH (30 wt%), EVA/ATH (65 wt%) and EVA/EG (10 wt%), respectively. Morphological comparisons, using microscopic and electronic microprobe analyses, revealed that 3D printed plates have lower apparent density and higher porosity than thermocompressed plate. The fire retardant properties of thermocompressed and 3D printed plates were then evaluated using Mass Loss Calorimeter test at 50 kW/m^2. Results highlight that 3D printing can be used to produce flame retardant systems. This work is a pioneer study

exploring the feasibility of using PAM technology for designing efficient flame retarded materials.

1. Introduction

Thermocompression (with also extrusion and injection molding) are usually used as polymer shaping process. It is an easy and widespread process, but the design of complex shapes is quite limited (because of the elaboration and the design of a mold beforehand). 3D printing or Polymer Additive Manufacturing (PAM) could be a solution to overcome this limitation [1]. Several 3D techniques have emerged these last years, such as for example: (i) Fused Deposition Modeling (FDM) (Figure 1 a) [1]-[4]; Selective Laser Sintering (SLS) (Figure 1 b), which uses a laser as the power source to sinter and bind powdered material to create a solid structure [5]-[7]; (ii) StereoLitography Apparatus ((SLA) with liquid or powder) [8], which is based on photopolymerization and therefore using light to link chains of molecules, forming polymers and thus making up a three dimensional solid (Figure 1 c).

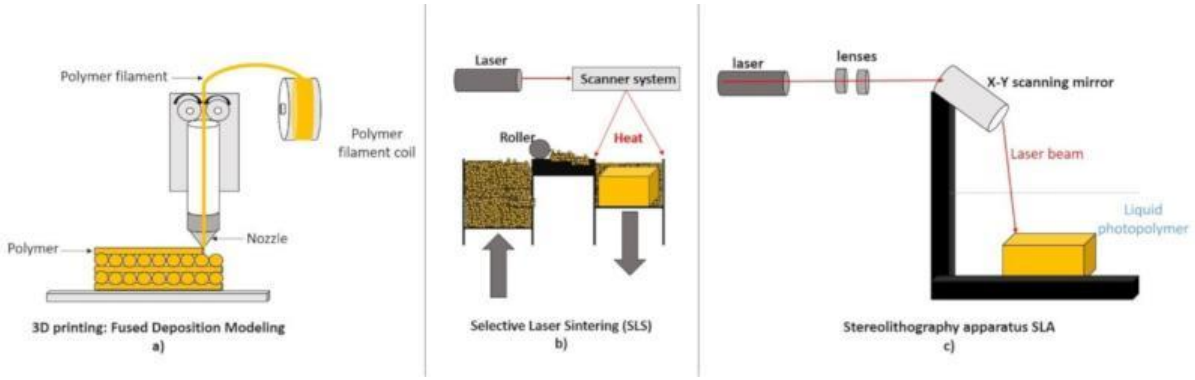

Figure 1. *Illustration of different 3D printing techniques (a) Fused Deposition Modeling (FDM), b) Selective Laser Sintering (SLS), c) StereoLitography Apparatus (SLA))*

Among these technologies, FDM presents the best quality to cost ratio. The principle consists in heating and softening a thermoplastic filament to deposit it on a substrate or support (Figure 1 a). The main limitation of this technology is the limited range of filaments commercially available. Moreover, the quality of printing can be disturbed by issues such as filament break, filament thickness and length, etc. [2], [4]. However, novel technologies, capable of printing raw materials from pellets and also of heating the receiving support or substrate [9], are now on the market. It has therefore many advantages compared to the technology using filaments, and this technique was used in this work. It indeed allows to suppress the winding step, and also to avoid issues associated to filament (break, diameter

restriction, …). Moreover, this 3D printer (like some others) has a heating plate, therefore, the adhesion of the 3D part during the printing is improved.

Literature is very scarce on the use of 3D printing in fire protection field [10], the main limitation being the capability to print flame retardant materials. The few papers recently published mainly focus on 3D printed polylactic acid (PLA) or acrylonitrile butadiene styrene (ABS), but none dealt with flame retarded Ethylene Vinyl Acetate (EVA) copolymer. The choice of EVA as model material (to prove a concept) makes sense because this is a polymer matrices well-known and study in our laboratory. In addition of that, this polymer is used in some sectors of industry, notably those concerned with aerospace, microelectronics, cable and wire manufacture are particularly interested in halogen free flame retarded EVA [11].

The main idea of this paper was to print flame retarded materials and to compare them with thermocompressed ones (Figure 2). Four polymers matrices were elaborated, namely neat EVA and EVA flame retarded with Aluminum TriHydroxyde (ATH) or expandable graphite (EG), and shaped using both thermocompression and 3D printing. All plates were characterized and compared quantitatively (mass, thickness and apparent density) and qualitatively by optical microscopy and Electron Microprobe (EPMA) analyses. Comparison of flame retardant properties of 3D printed and thermocompressed plates were carried out by mass loss calorimeter test (MLC) using an external heat flux of 50 kW/m².

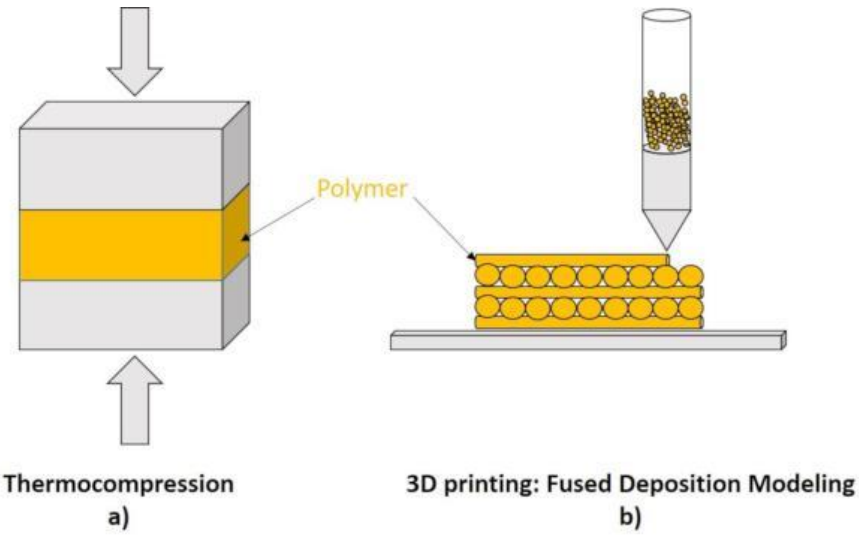

Figure 2. *Illustration of (a) thermocompression vs (b) 3D printing by FDM*

2. Materials and Methods

2.1. Materials

100x100x3 mm^3 polymer plates were shaped by thermocompression and 3D printing process. Figure 3 summarizes all processing steps used to make the materials. Each step will be detailed afterwards.

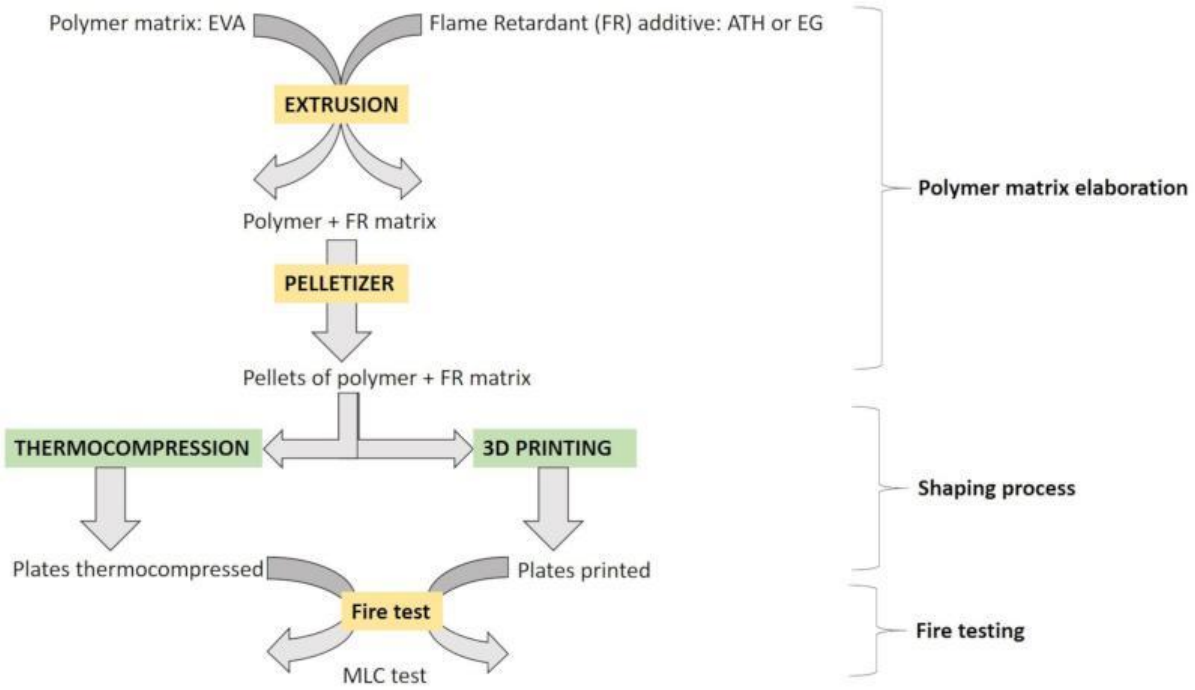

Figure 3. *Illustration of the whole experimentation*

2.1.1. Processing

EVA (Evatane 28-05) purchased from Arkema (Colombes, France) (batch A70760804) was used as polymeric matrix because of its softness, flexibility and polarity, which makes it easy to extrude. Flame retardant additives incorporated in EVA were: Expandable Graphite (EG) ES 350F5 purchased from AMG graphite (Hauzenberg, Germany) (80% of EG particles are higher than 300 µm), and Aluminum Trihydroxide Hydrate (ATH) Apyral 40CD purchased from Nabaltec (Schwandorf, Germany) (ATH particles size D_{50} is 1.5µm). These two flame retardant additives were chosen because of their different behavior upon heating. Indeed, EG has a physical "worm" expansion due to the expansion of graphite, caused by the sublimation of inserted compounds trapped between the graphite layers [12] - [15]. On the opposite, ATH dehydrates endothermally upon heating coupled with a dilution effect (water evolution into the

gas phase) and the formation of ceramic-like residue (alumina) acting as protective layer [16]. Four materials were prepared (Table 1).

Table 1. *Materials' formulation*

Polymer matrix	Amount of additives (wt%)	Thermal behavior
EVA	0	Reference: melting and burning
EVA/ATH (30 wt%)	30	Endothermic decomposition and dilution effect: ceramic residue
EVA/ATH (65 wt%)	65	Endothermic decomposition and dilution effect: ceramic residue
EVA/EG	10	Physical expansion [12]

The filled EVA were produced by extrusion (Thermo Scientific Rheomex Haake (Vreden, Germany). First, EVA pellets and different amounts of ATH (30 wt% and 65 wt%) or EG (10 wt%) were melted and mixed using a twin-screw extruder (Thermo Scientific Rheomex OS PTW16 Haake (Vreden, Germany). The polymer and additive incorporation was done using gravimetric dosing. The temperatures of the 10 heating chambers were: 150°C (polymer and additive feed area) – 160 °C – 160 °C – 160 °C (additive insertion area) – 170 °C – 170 °C – 170 °C – 160 °C – 160 °C – 150 °C, from funnel to extrusion head respectively. The extrusion speed was 100 and 250 rpm for EVA/ATH and EVA/EG respectively. After extrusion, the filaments of EVA/ATH or EVA/EG were cooled down under air and cut into pellets with a pelletizer (Thermo Scientific (Waltham, Massachusetts, United States of America)).

The pellets were then used to produce plates by two processes: thermocompression and 3D printing. These two processes are described in the next sections.

2.1.2. Thermocompression shaping process

100x100x3 mm^3 plates were produced by thermocompression process, using Fontune presses supplied by Fontijne Grotnes B.V. (Niles, Michigan, United States). A defined mass of polymer pellets was put in a mold, allowing to obtain a plate. The following simultaneous temperature and pressure cycles were applied: the pellets were heated at 140 °C for 14 min then cooled at 30 °C for 1 min meanwhile a force was set to 20 kN for 3 min, then 40 kN for 12 min. Plates hereafter named T-EVA, T-EVA/ATH (30 wt%), T-EVA/ATH (65 wt%), and T-EVA/EG (10 wt%), were prepared and their total thicknesses were 3 mm ± 0.2 mm (Table 3).

2.1.3. 3D printing shaping process

100x100x3 mm^3 plates were produced by 3D printing process, using PAM (Polymer Additive Manufacturing) Series P supplied by Pollen (Ivry-sur-Seine, France), which is a Fused Deposition Modeling (FDM) printer, capable of printing materials as pellets (Figure 4) [9]. Twelve temperature control points located in the print head ensure that the polymers are exposed to negligible shear forces and residence time. Finally, this 3D printing has 4 extruders, enabling to print a multi-material up to 4 on a single part.

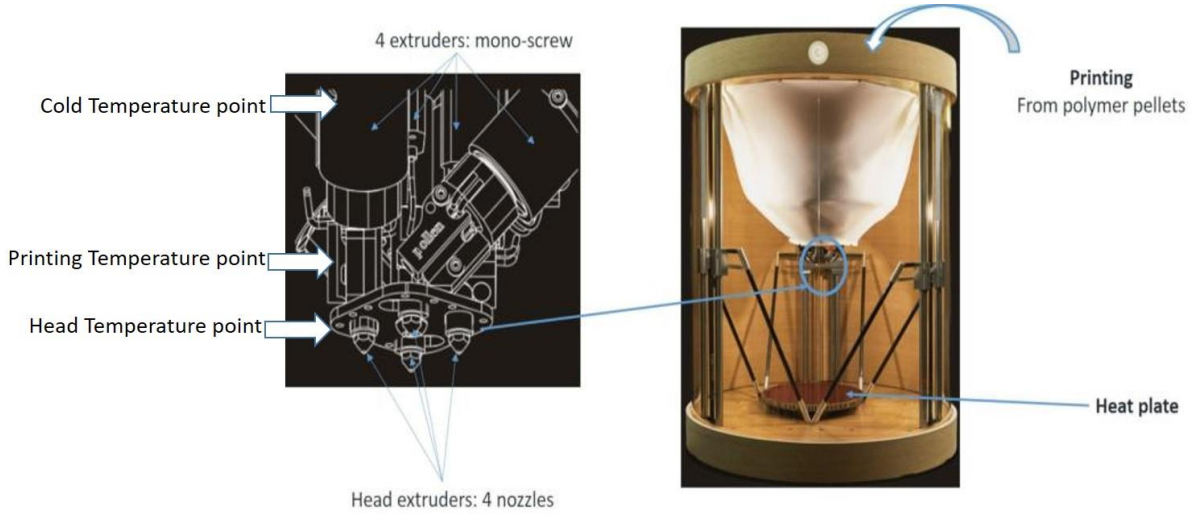

Figure 4. *Description of 3D printing used [9]*

The 3D plates shaping is divided into three steps, illustrated in Figure 5. First, a 3D part conception is done on Catia V5 (Computer-Aided Three-Dimensional Interactive Application) software. This is a multi-platform software suited for computer-aided design, which allows 3D conception. When the object is virtually elaborated, with the right dimension, the file is exported to another software named Ultimaker Cura. Using this software, the 3D part is sliced in many sections, corresponding to the layers that will be printed. This second step is the most important, as it allows defining all printing parameters, guaranteeing a good quality of printing. Then, the file is exported on a last software: Pollen, which allows to start or stop the printing. Before starting the printing, the polymer cartridge has to be filled in with polymer pellets.

Figure 5. 3D printed process

Main printing parameters defined to elaborate the four materials are reported in Table 2. It is possible to notice that nozzle diameter is higher for EVA/EG (10 wt%) (1 mm) compared to other materials (0.4 mm), due to the higher particles size (150 µm against 300 µm for EVA/ATH and EVA/EG respectively). Moreover, three temperature points (figure 4) are important to define: i) cold temperature, which corresponds to a polymer pellets temperature before extrusion, ii) printing temperature, which is the temperature in extruder, and iii) head temperature which corresponds to a nozzle temperature (polymer output). Bed temperature allows to get the appropriate adhesion between fused polymer and plate. This parameter depends on filler amount and composition. All of the 3D printed plates have 100% infill to be well compared to thermocompressed plates. Using this whole process, plates were prepared and shaped. They were named 3D-EVA, 3D-EVA/ATH (30 wt%), 3D-EVA/ATH (65 wt%), and 3D-EVA/EG (10 wt%), and their total thicknesses were 3.15 mm ± 0.15 mm (Table 3).

Table 2. Printing parameters

Polymer matrix	EVA	EVA/ATH (30 wt%)	EVA/ATH (65 wt%)	EVA/EG (10 wt%)
Cold temperature (°C)	65	65	65	65
Printing temperature (°C)	130	130	130	130
Head temperature (°C)	230	225	220	200
Printing speed (mm/s)	30	20	30	30
Nozzle diameter (mm)	0.4	0.4	0.4	1
Bed Temperature (°C)	45	65	80	65
Infill (%)	100	100	100	100
Layer height	0.3	0.3	0.3	0.3

2.2. Fire test: Mass Loss calorimeter (MLC)

The selected laboratory scale fire test, named Mass Loss Calorimeter (MLC) consists in exposing the 100x100x3 mm^3 samples to a 50 kW/m^2 radiative heat flux (scenario corresponding to a fully developed fire). This fire testing technology follows the procedure defined in ISO 13927 standard. The samples were placed in horizontal orientation on a load cell distant from 35 mm from the cone heater. Forced ignition was used (Figure 6), [17] - [21]. This fire test is similar to cone calorimeter test described in ISO 5660, except that the Heat Release rate (HRR) is measured, after a calibration step with methane, using a thermopile (constituted of four thermocouples) located at the top of a chimney instead of oxygen consumption. Data were collected and analyzed using MLC Calc software (Radcal, Monrovia, California, United States of America).

Several parameters are obtained after MLC tests and allow estimating the fire behavior of sample exposed: i) HRR plotted versus time to obtain the thermal behavior of materials; ii) Total Heat Release (THR), which corresponds to the area under the HRR versus time curves; iii) Peak of Heat Release Rate (PHRR), which is one of the critical factors in predicting the growth rate of fire; iv) Time To Ignition (TTI), which is the time until sample is ignited. Experiments were performed in triplicate to ensure repeatability of obtained results. They were repeatable within 10%.

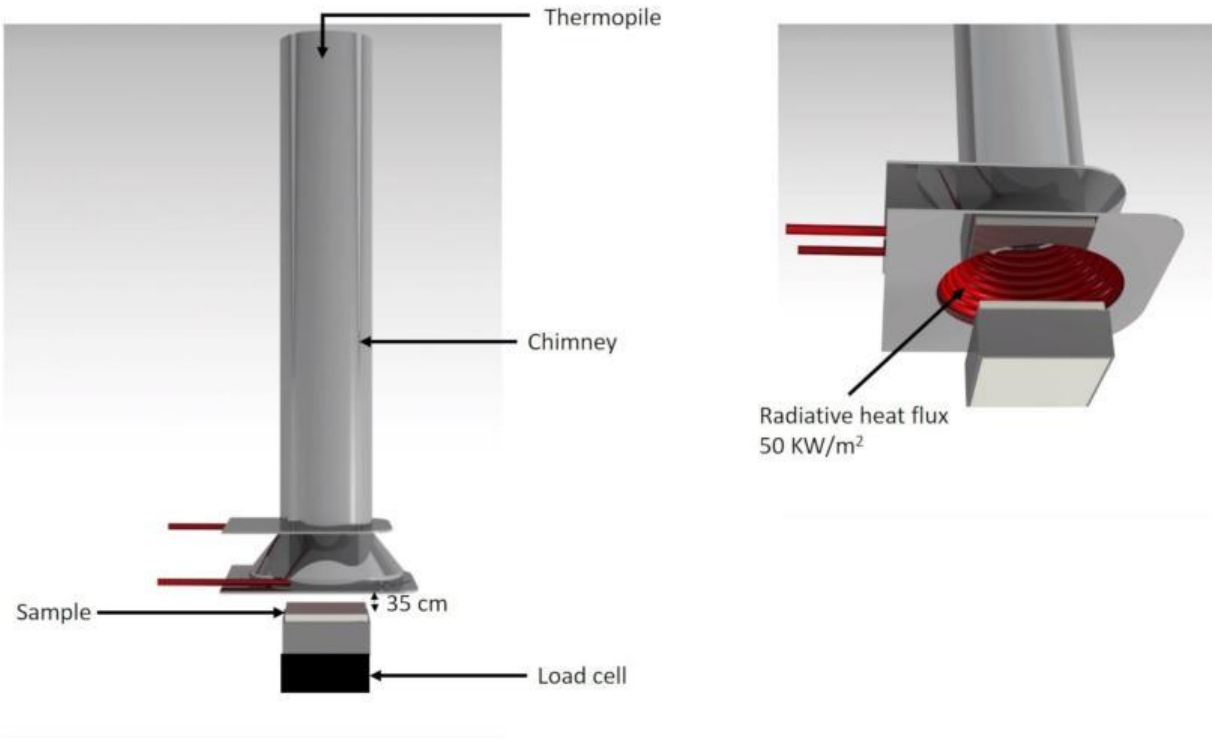

Figure 6. *Description of Mass Loss Calorimeter (MLC) test*

2.3. Characterizations

2.3.1. Quantitative and qualitative characterizations

Thicknesses of samples were measured using a numerical caliper. Samples volume and apparent density were calculated using formula 1: length (mm) x width (mm) x thickness (mm)) and formula 2: weight (kg) divided by volume (m^3), respectively.

Before fire test, optical microscopy observations were carried out on 1x1 cm^2 thermocompressed and 3D printed samples using a microscope VHX-1000 HDR (High Dynamic Range), Keyence (Osaka, Japan). Top and cross section analyses were carried out to evaluate the morphology differences between the two processes depending on the samples studied. Therefore, each sample was put in liquid nitrogen for 5 min and then cut using a blade and a hammer. Using this protocol, a brittle fracture was obtained without affecting the integrity of the sample. The cross-cut samples obtained were embedded in an epoxy resin, dried for 48h at room temperature, and polished (up to ¼ µm) using silicon carbide disks (ESCIL, Chassieu, France) to obtain the smoothest surface as possible to facilitate observations.

Before fire testing, cross section X-ray mappings of 3D printed and thermocompressed plates were carried out to examine the FR additive repartition and dispersion. The cross-cut samples (see previous section) were embedded into epoxy resin, polished and carbon coated with a Bal-Tec SCD005 sputter coater (Bal-Tec, Los Angeles, California, United States). A Camera SX100 electron probe microanalyser (EPMA) (Cameca, Gennevilliers, France) was used to perform elemental analysis. Back scattered electron (BSE) images and X-ray mappings were carried out at 15 kV, 40 nA. For mappings, the crystals used to detect the K□ of C, Al and S were a PC2 (a multilayer of Ni/C), a Thallium Acid Phthalate (TAP), and Pentaerythritol (PET) respectively. S element was chosen as element to detect in EVA/EG (10 wt%) because of the presence of H_2SO_4 and HNO_3 as insertion compounds in expandable graphite. The mappings are color-coded from black to red, with black characterizing the absence of the element and red the highest concentration detected.

2.3.2. Thermal conductivity measurements

Thermal conductivity of T-EVA/EG (10 wt%) and 3D-EVA/EG (10 wt%) was measured at room temperature by a hot disk thermal constant analyser (Hot Disk TPS 2500S) from Thermoconcept (Bordeaux, France), which is a transient plane source technique [22]. The sensor (warmth emitter) is mould in the middle of two samples (25 x 25 x 6 mm^3) to ensure a good contact during the experiment. The conductivity measurements were carried out by

applying a power of 0.06 and 0.065 W for 10s for T-EVA/EG (10 wt%) and 3D-EVA/EG (10 wt%), respectively. The experiment was repeated four times to check the repeatability of the measurement. The presented results are the average of the obtained values.

3. Results and discussion

3.1. T and 3D-materials before fire testing

A quantitative comparison between thermocompressed and 3D printed plates was firstly carried out in terms of mass, thickness, volume and apparent density (Table 3). According to Table 3, whatever the material, standard deviation between each sample is very small (lower than 5 g, 0.3 mm, 154 kg/m^3 for weight, thickness and apparent density respectively). Therefore, the three samples are comparable for each material studied. Moreover, the thickness and mass differences between thermocompressed and 3D printed plates were calculated for each material and correspond to 5%, - 7%, 14%, and 1%, and 1%, - 14%, 7%, and - 8% for EVA, EVA/ATH (30 wt%), EVA/ATH (65 wt%), and EVA/EG (10 wt%) respectively. Considering the only slight differences between values (relative error is lower than 15%), the thermocompressed and 3D printed plates can therefore be considered as similar in size. In addition to that, the apparent density difference between thermocompressed and 3D printed plates was estimated for each material studied and corresponds to - 5%, - 11%, - 4%, and - 9% for EVA, EVA/ATH (30 wt%), EVA/ATH (65 wt%) and EVA/EG (10 wt%) respectively. As it was shown above, relative error between thermocompressed and 3D printed plate is lower than 15%, which is considered as acceptable. Therefore, thermocompressed and 3D printed plates are considered quantitatively comparable, whatever the polymeric material studied.

Table 3. *Thermocompression vs 3D printing: samples comparison before fire test*

Samples	Mass (g)			Thickness (mm)			Apparent density (kg/m³)		
	T	3D	Δ%	T	3D	Δ%	T	3D	Δ%
EVA	27.5±0.1	27.9±0.9	1	2.94±0.02	3.1±0.1	5	938±3	890±1	-5
EVA/ATH (30 wt%)	35±1	30±5	-14	3.15±0.09	3.02±0.07	-7	1151±43	1026±154	-11
EVA/ATH (65 wt%)	44±2	47±4	7	2.9±0.1	3.3±0.3	14	1517±4	1449±14	-4
EVA/EG (10 wt%)	30.85±0.01	28.3±0.4	-8	3.099±0.005	3.12±0.01	1	996±1	906±10	-9

Based on these results, a morphological analysis was carried out and is presented in the next section.

3.2. Morphological analysis before fire test

Surface and cross section microscopic analyses were carried out on thermocompressed and 3D printed plates using optical microscopy and EPMA observations.

3.2.1. Surface characterizations

Thermocompressed and 3D printed plate surfaces were compared by optical microscopy, the resulting pictures are gathered in Figure 7. In each case, the top surfaces of the material look different depending on the formulations and on the process. It is noteworthy the 3D printed plate surfaces are rougher than the thermocompressed ones. This difference is due to the juxtaposition of the filaments deposited at each nozzle passage during 3D printing. The polymer filament diameter was measured for each material studied using optical microscopy (Figure 7) and it is directly linked to the nozzle diameter used for printing. The filaments have indeed diameters of 400 µm, 400 µm and 1000 µm for 3D-EVA, 3D-EVA/ATH (with 30 wt% and 65 wt%), and 3D-EVA/EG (10 wt%) respectively corresponding to the nozzle diameters (Table 2).

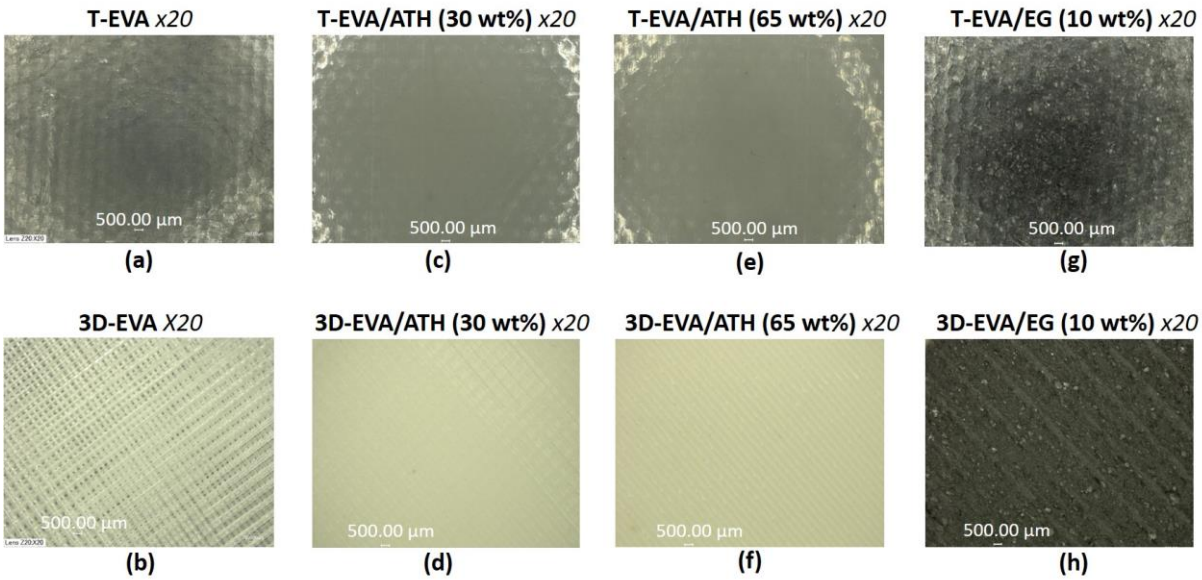

Figure 7. *Surface observations of thermocompressed and 3D printed samples using optical microscopy x20 (a) T-EVA, b) 3D-EVA, c) T-EVA/ATH (30 wt%), d) 3D-EVA/ATH (30 wt%), e) T-EVA/ATH (65 wt%), f) 3D-EVA/ATH (65 wt%), g) T-EVA/EG (10 wt%), h) 3D-EVA/EG (10 wt%))*

3.2.2. Cross-section analyses

Cross-section observations using optical microscopy and EPMA were carried out on all thermocompressed and 3D printed samples studied (Figures 8, Figure 9, Figure 10, Figures A1

and A2), to evaluate and compare the porosity and fillers dispersion. For neat EVA, some small pores are clearly detected in 3D-EVA plates with diameters between 115 and 500 µm, compared to T-EVA, in which no pore can be distinguished (Figure 8 a, Figure 8 b and Figure A1). For 3D-EVA/ATH (30 wt%), small pores with diameters approximatively between 35 and 115 µm are observed (Figure 8 d and Figure A2), whereas no pores are noticed for T-EVA/ATH (30 wt%) (figure 8 c). With a higher ATH ratio (65 wt%), no pores are detected, whatever the shaping process used (T or 3D), as observed in Figure 8 e, Figure 8 f and Figure A2. This difference between 30% and 65% filled samples could be explained by the higher density of the material containing the higher ATH amount. Indeed, it is possible to assume that ATH particles (with a quite low diameter (1.5 µm)) collapse pores. Finally, cross section X-Ray mappings in Al element (Figure 9) show that no difference is observed between thermocompressed and 3D printed materials, whatever the ATH ratio used.

Regarding 3D-EVA/EG (10 wt%), some small pores with diameters approximatively between 100 and 200 µm are observed (Figure 8 h), whereas no pores are noticed for T-EVA/EG (10 wt%) (Figure 8 g). Therefore, in most cases, and as already reported in the literature [23], 3D plates show higher porosity compared to those obtained with the thermocompression process (Figure 8 and Figure A1 and A2). This porosity caused with 3D printing shaping process is explained by the thin melting polymer filaments which are deposed successively to form a 3D model.

Moreover, for 3D-EVA/EG (10 wt%), 3D-EG particles appear smaller than T-EG particles. Indeed, average length of 3D-EG particles is 116 µm compared to 263 µm for T-EG. This length difference between both shaping process (T vs 3D) could be explained by the second extrusion run. It causes that particles could be cut by shear stresses during extrusion. Moreover, the small nozzle diameter in 3D printing process (1 mm for EVA/EG (10 wt%)) could also justify this length difference. On top of that, 3D-EG particles seem to be aligned (Figure 8 h) while to T-EG particles exhibit a random distribution (Figure 8 g). These observations are confirmed by the cross section X-ray mapping of S element in Figure 10. This preferential orientation can be explained by the nozzle moving and the juxtaposition of the filaments deposited at each nozzle passage during the 3D printing.

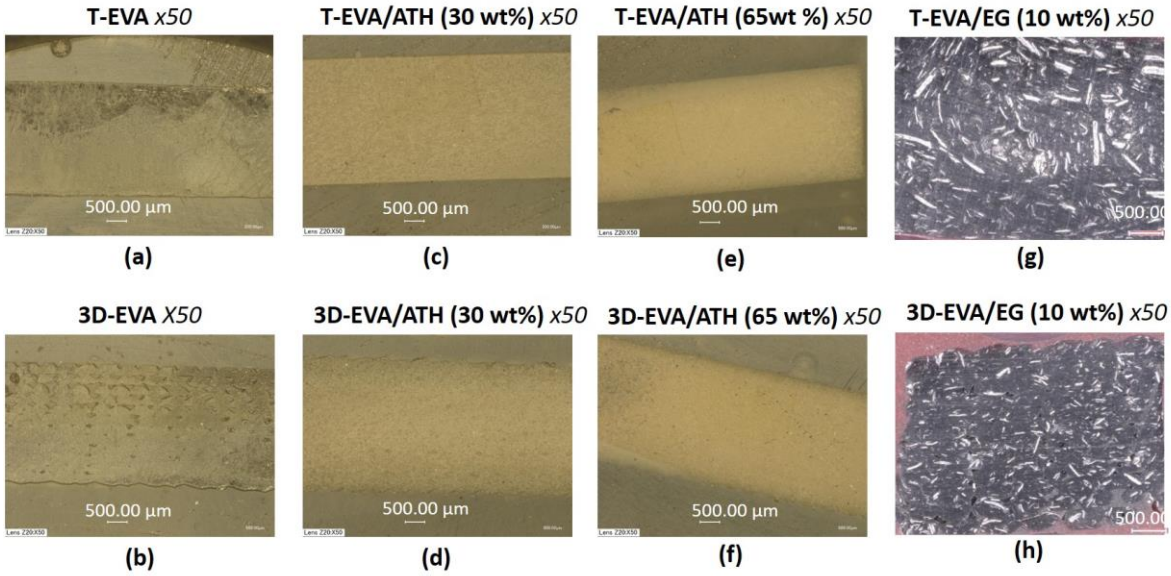

Figure 8. *Cross-section observations of thermocompressed and 3D printed samples using optical microscopy x50 (a) T-EVA, b) 3D-EVA, c) T-EVA/ATH (30 wt%), d) 3D-EVA/ATH (30 wt%), e) T-EVA/ATH (65 wt%), f) 3D-EVA/ATH (65 wt%), g) T-EVA/EG (10 wt%), h) 3D-EVA/EG (10 wt%))*

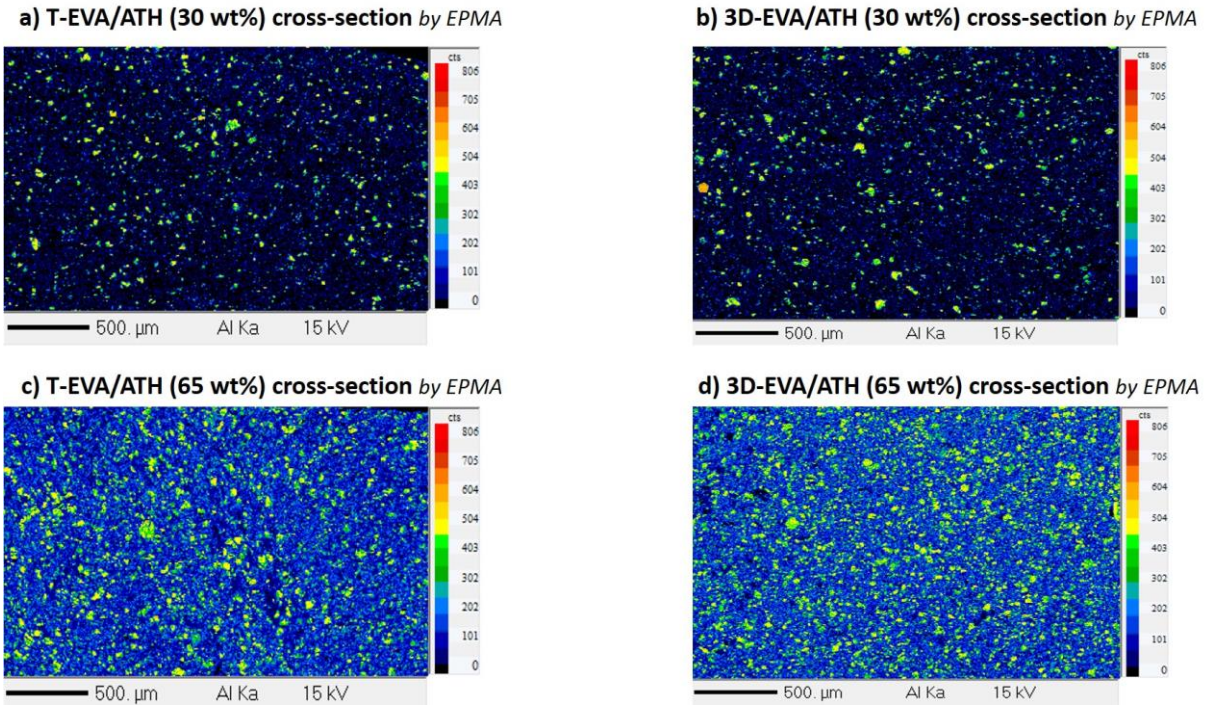

Figure 9. *Cross section X-ray mapping in Al element using EPMA measurements of (a) T-EVA/ATH (30 wt%), b) 3D-EVA/ATH (30 wt%), c) T-EVA/ATH (65 wt%), d) 3D-EVA/ATH (65 wt%))*

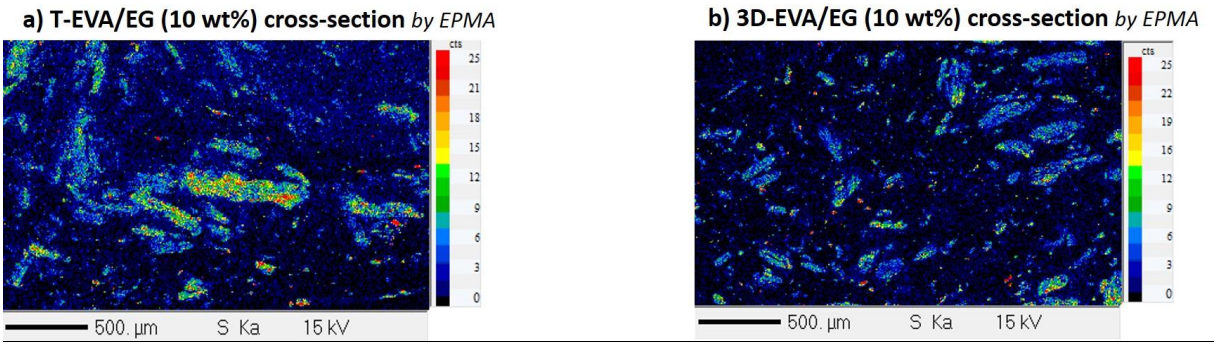

Figure 10. *Cross-section X ray mapping in S element using EPMA measurements of (a) T-EVA/EG (10 wt%), b) 3D-EVA/EG (10 wt%))*

In the next section the flame retardant properties of 3D printed and thermocompressed samples will be compared.

3.3. Fire behavior

Fire retardant performances of 3D-EVA, 3D-EVA/ATH (30 wt%), 3D-EVA/ATH (65 wt%), and 3D-EVA/EG (10 wt%) were compared to those of T-EVA, T-EVA/ATH (30 wt%), T-EVA/ATH (65 wt%), and T-EVA/EG (10 wt%)). Figure 11 and Table 4 report the heat release rate (HRR) curves and the main values measured during the test (TTI, THR, and pHRR) respectively. In all cases, the pHRR and THR are dramatically reduced by the addition of ATH and EG (Figure 11). The highest fire retardant performances are observed with EVA/ATH (65%) (THR and pHRR are reduced by 49 % and 78 % respectively and TTI is increased by 72% compared to neat EVA) and EVA/EG (10 wt%) (THR and pHRR are decreased by 17 % and 70 % respectively, in comparison with neat EVA). As regards EVA/ATH (30 wt%), a slightly reduction of pHRR (23%) is noticed compared to neat EVA, but no improvement of THR and TTI are observed. For EVA/EG (10 wt%), the FR properties are explained by a physical “worm” expansion, due to the expansion of graphite, as it was expected. Regarding EVA/ATH material, an endothermal dehydration occurs upon heating, leading to the formation of a ceramic-residue (alumina). A critical amount of ATH is needed to obtain an efficient homogenous residue, which then acts as a fire barrier. This explains why EVA/ATH (65 wt%) shows higher fire retardant performances than EVA/ATH (30 wt%).

Moreover, whatever the shaping process (thermocompression or 3D printing), EVA (Figure 11 a), EVA/ATH (30 wt%) (Figure 11 b) and EVA/ATH (65 wt%) (Figure 11 c) have similar fire behavior. The THR difference between thermocompressed and 3D printed plates corresponds to only 3 %, - 12 % and 8 % (2 MJ/m^2, 9 MJ/m^2 and 3 MJ/m^2), for EVA, EVA/ATH (30 wt%) and EVA/ATH (65 wt%) respectively: it lies in the margin of errors and they cannot be considered as significant. In the same manner, pHRR differences between

thermocompressed and 3D printed plates are quite small (37 kW/m² for EVA, 38 kW/m^2 for EVA/ATH (30 wt%) and 12 kW/m² for EVA-ATH (65 wt%) (also in the margin of error: - 7 % - 9 % and - 11%). Therefore, it can be concluded that shaping process has no particular influence on fire behavior for these two matrices. However, for EVA/EG (10 wt%), differences are noticeable: thermocompressed plates show improved flame retardant properties compared to the 3D shaped ones. THR difference between thermocompressed and 3D printed plates is indeed 12 MJ/m^2, corresponding to 19 % difference. Moreover, the pHRR difference for the same formulation is 61 kW/m^2 (i.e. 39 %). Regarding the ignition time, it is quite similar between thermocompressed and 3D printed plates, whatever the materials studied (Table 4).

To sum up the fire behavior, THR and pHRR are similar between thermocompressed and 3D printed plates except for EVA/EG (10 wt%). Indeed, in this case, 3D printing process impairs fire properties, as pHRR and THR both increase (+ 39 % and + 19 %) for the 3D printed samples.

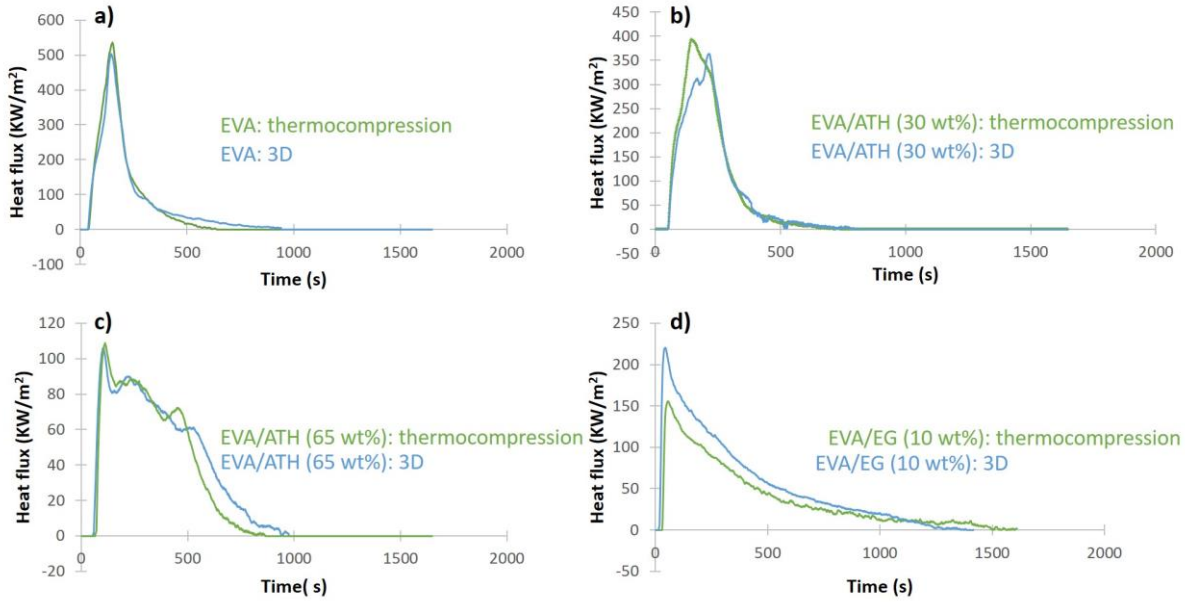

Figure 11. *Fire behavior comparison between thermocompression and 3D printing process (a) EVA, b) EVA/ATH (30 wt%), c) EVA/ATH (65 wt%), d) EVA/EG (10 wt%))*

Table 4. *Comparison of MLC results between thermocompression and 3D printing process depending on the polymer matrix studied*

Samples	Ignition time (s)			THR (MJ/m²)			pHRR (kW/m²)		
	T	3D	Δ%	T	3D	Δ%	T	3D	Δ%

EVA	40±0	35±4	-13	76±6	78±5	3	519±26	482±31	-7
EVA/ATH (30 wt%)	37±4	31±5	-16	77±4	68±12	-12	401±15	363±18	-9
EVA/ATH (65 wt%)	65±5	58±4	-11	39±0.1	42±2	8	113±5	101±10	-11
EVA/EG (10 wt%)	21±2	18±1	-14	63±5	75±2	19	156.0±0.2	217±4	39

Pictures of the residues obtained after MLC testing are gathered in Figure 12. For each system, and whatever the shaping process, residues have the same visual aspect. EVA burns completely and does not yield any residue. For EVA/ATH (30 wt%) and EVA/ATH (65 wt%) samples, a ceramised residue is obtained with similar visual aspect (Figure 12), regardless the shaping process. Same conclusion can be made regarding the visual aspect of EVA/EG (10 wt%) residues. Indeed, a "worm-like" expansion occurs in both cases. Therefore, shaping process (thermocompression vs 3D printing) has no influence on the visual aspect of the residue for each polymer matrix studied.

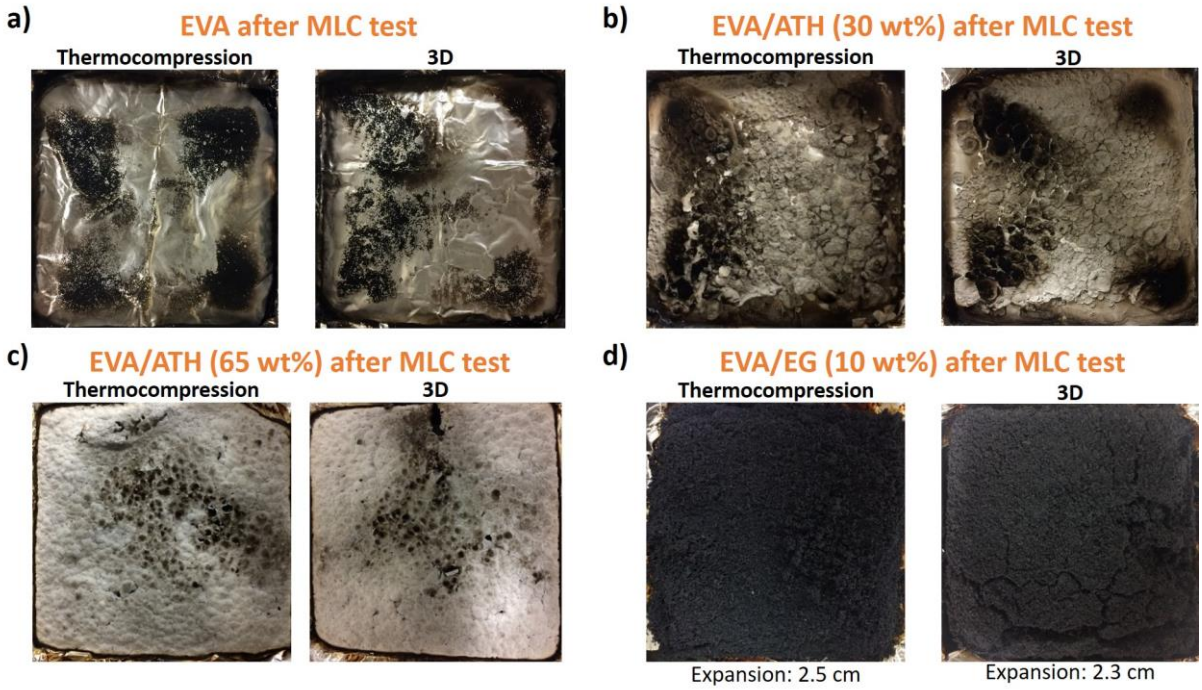

Figure 12. *Visual aspect of residues after MLC test for (a) EVA, b) EVA/ATH (30 wt%), c) EVA/ATH (65 wt%), and d) EVA/EG (10 wt%))*

During MLC experiment, the residual weight after fire test was also measured for each sample and results are presented in Table 5. For EVA and EVA/ATH (30 wt%), the same

residual weight is obtained, whatever the shaping process used. But, for EVA/ATH (65 wt%) and EVA/EG (10 wt%) a difference is measured between thermocompressed and 3D printed plates. This difference reaches 4 % between T-EVA/ATH (65 wt%) and 3D-EVA/ATH (65 wt%) (which is considered as negligible) and 42 % between T-EVA/EG (10 wt%) and 3D-EVA/EG (10 wt%). This residual mass difference after fire test is related to the difference observed in term of fire retardant performance between 3D and thermocompressed plates, as previously highlighted.

Table 5. *Comparison of residual mass after MLC test for thermocompression and 3D printed plates*

Samples	Residual weight (g)	Residual weight/initial weight (%)	Δ Residual mass (thermocompressed vs 3D) (%)
T-EVA	0±0	0	0
3D-EVA	0±0	0	
T-EVA/ATH (30 wt%)	6.8±0.3	19	0
3D-EVA/ATH (30 wt%)	6±1	19	
T-EVA/ATH (65 wt%)	22.4±0.9	49	4
3D-EVA/ATH (65 wt%)	21.2±1.9	47	
T-EVA/EG (10 wt%)	7.3±0.09	24	42
3D-EVA/EG (10 wt%)	3.9±0.08	14	

Figure 13 summarizes the thermal behavior of the different materials. EVA, EVA/ATH (30 wt%) and (65 wt%) show the same thermal behavior (and same residual aspect and mass), no matter the shaping process used. When EVA undergoes radiative heating (MLC test), the polymer melts immediately (pores which were created by 3D printing collapse) and burns (Figure 13 a) or ceramizes (if containing ATH) (Figure 13 b). For EVA/EG (10 wt%), the fire behavior is worse for 3D printed plates than for thermocompressed ones. The differences between 3D and T-EVA/EG (10 wt%) materials could be explained by three-factors: (1) the EG particles size, lower after 3D printing. These smaller EG particles lead to lower graphite expansion [24], to a less cohesive entangled network and thus to lower thermal protective performances (Figure 13 c); (2) the higher porosity observed in the 3D printed materials might also decrease the cohesion of the entangled network, thus damaging the fire protective

properties of 3D-materials compared to T-materials; (3) Finally, it was previously reported that 3D-EG particles have a preferential orientation, leading to an anisotropic material (Figure 14 b), compared to an isotropic thermocompressed one (Figure 14 a) [25]. This morphological difference could also partly explain the lower thermal protective performance of 3D-EVA/EG (10 wt%). Indeed, when the physical "worm" expansion occurs, it is assumed that graphite expansion differs depending on the EG orientation. Moreover, influence of the first factor (higher porosity of 3D sample) on the thermal behavior is confirmed by the thermal conductivities of T-EVA/EG (10 wt%) and 3D-EVA/EG (10 wt%) equal to 0.451 ± 0.002 W/mK and to 0.241 ± 0.001 W/mK respectively. Thus, the thermal conductivity of the 3D sample is divided per almost two compared to that of thermocompressed one. This result makes sense because of the low thermal conductivity of gases (encapsulated air): the higher the porosity, the lower the thermal conductivity [26]. Therefore, based on these three hypotheses, the entangled network is differently organized in both cases, which could explain the thermal behavior differences.

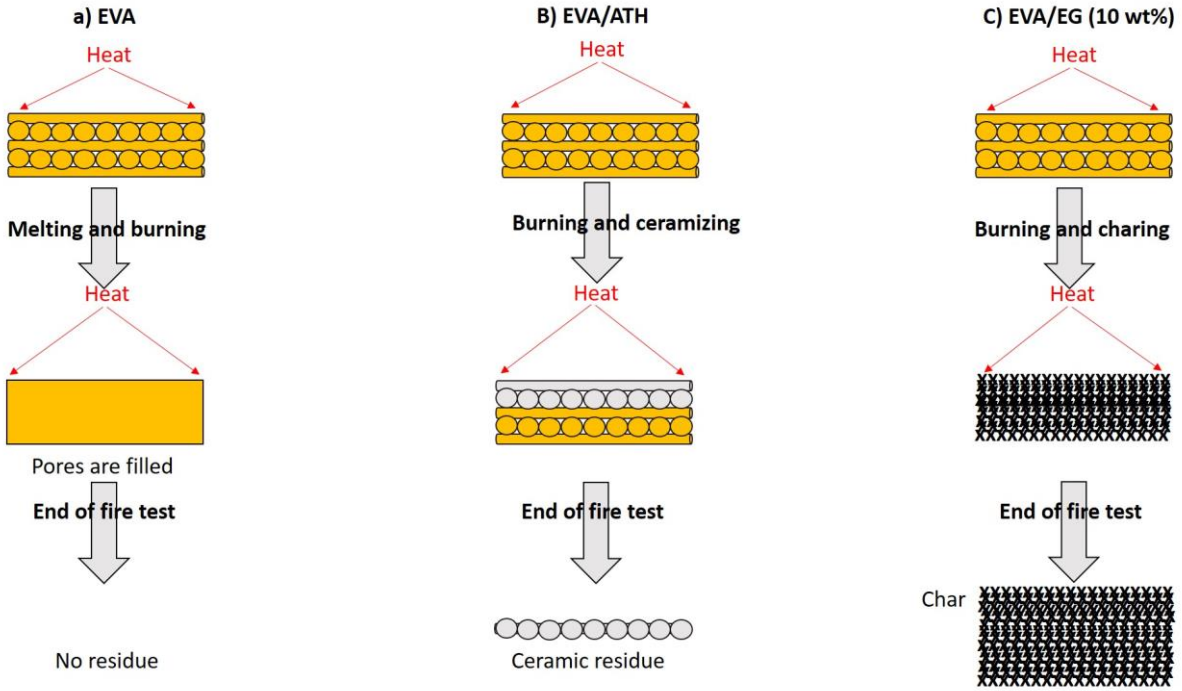

Figure 13. *Illustration of the 3D printed polymer matrices thermal behavior(a) EVA, b) EVA/ATH, c) EVA/EG (10 wt%))*

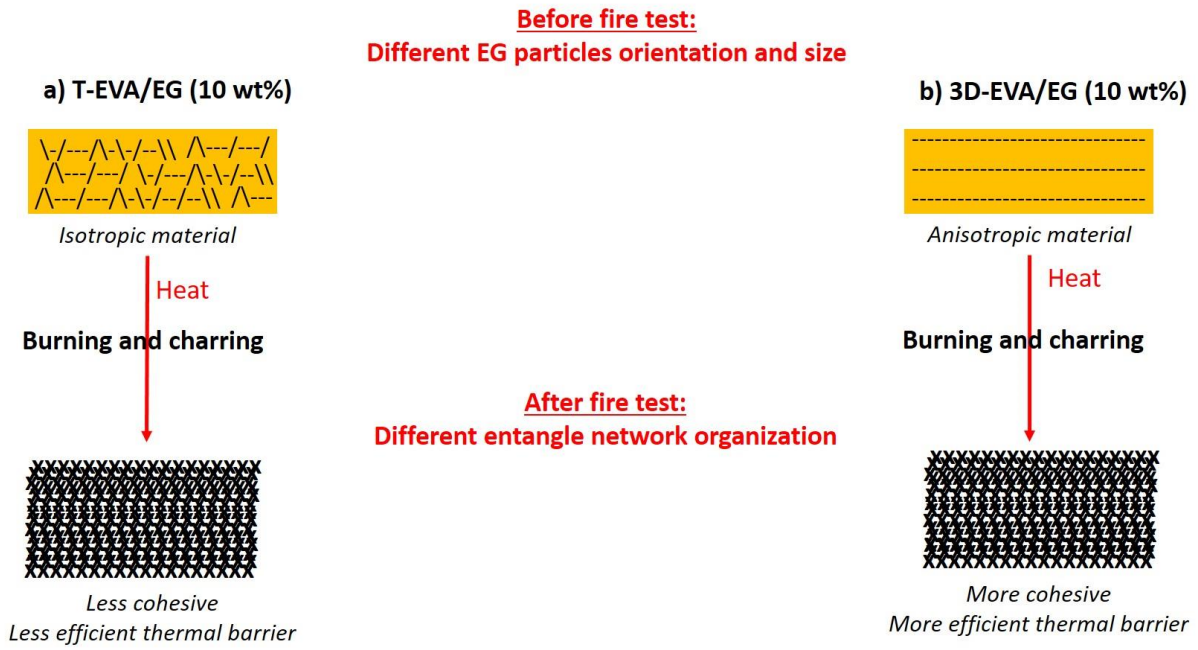

Figure 14. *Illustration of EVA/EG (10 wt%) thermal behavior (a) Thermocompressed plates, b) 3D printed plates)*

Conclusion

This work compared two shaping process, i.e. thermocompression and 3D FDM, to design flame retardant systems. Results show that it is possible to design flame retardant matrices by 3D printing, and that the fire behavior is not particularly affected by the shaping process. The porosity inherent to the successive filaments deposition during the 3D printing process, has no influence on the burning mechanism of the polymer matrices. However, nozzle size and "re-extrusion" of the filaments inside the 3D printer can have some harmful influence on some flame retardant fillers, such as expandable graphite. For example, the smaller size of the EG particles as well as the horizontal preferential orientation induced by filaments deposition, lead to decreased fire-retardant properties of the 3D printed plates compared to thermocompressed ones. This work however proves that 3D printing promising way to design flame retarded polymers, leading to a new way of thinking for flame retardant community: improve flame retardancy by design modification rather than just by playing with materials chemistry.

Author Contributions

S.B., M.J. and F.S. supervised the work, discussed the results and contributed to the paper writtten by L.G. L.G. carried out the thermocompressed and 3D printed plates elaboration and

characterization by optical microscopy. She also analyzed EPMA measurements (with Dr. Séverine Bellayer help) of the samples and performed and analyzed all the thermal tests (MLC). She performed the scientific discussion and conclusions and wrote the paper.

Funding

This work has received funding from the European Research Council (ERC) under the European Union's H2020- the framework programme for Research and Innovation (2014-2020) ERC Grant Advances Agreement N°670747-ERC 2014 AdG/FireBar-Concept for FireBar Concept project.

Acknowledgements

We would also like to thank Johan Sarazin for his help during the printing profile determination, and Dr. Séverine Bellayer for the EPMA measurements and observations.

References

[1] C. Mota, D. Puppi, F. Chiellini, and E. Chiellini, "Additive manufacturing techniques for the production of tissue engineering constructs," *J. Tissue Eng. Regen. Med.*, no. November 2012, pp. 174–190, 2015, DOI : 10.2002/term.1635

[2] Grasso, M.; Colosimo, B.M. Process defects and in situ monitoring methods in metal powder bed fusion: A review. Meas. Sci. Technol. 2017, 28, 1–25, DOI: https://doi.org/10.1088/1361-6501/aa5c4f

[3] Zhong, Y.C.; Ahn, I.H.; Moon, S.K. Process monitoring and inspection systems in metal additive manufacturing: Status and applications. Int. J. Precis. Eng. Manuf. Green Technol. 2017, 4, 235–245, DOI: https://doi.org/10.1007/s40684-017-0029-7

[4] Z. Yang, "Filament Breakage Monitoring in Fused Deposition Modeling Using Acoustic Emission Technique," *Sensor*, pp. 1–16, 2018, doi: 10.3390/s18030749.

[5] K. F. Leong, K. K. S. Phua, C. K. Chua, Z. H. Du, and K. O. M. Teo, "Fabrication of porous polymeric matrix drug delivery devices using the selective laser sintering technique," *Proc Inst Mech Eng H*, vol. 215, pp. 191–201, DOI:10.1243/0954411011533751

[6] P. E. A. Powell, "Selective laser sintering with assisted powder handling.," 1990.

[7] M. Savalani, L. Hao, Y. Zhang, K. E. Tanner, and R. A. Harris, “Fabrication of porous bioactive structures using the selective laser sintering technique,” *Proc Inst Mech Eng H*, vol. 221, pp. 873–886, 2007, DOI: 10.1243/09544119JEIM232

[8] P. J. Ba, *Stereolithographic Processes*. 2011.

[9] pollen society, “Pollen AM _ Pellet Additive Manufacturing.”.

[10] Y. Guo *et al.*, “Engineering flame retardant biodegradable polymer nanocomposites and their application in 3D printing,” *Polym. Degrad. Stab.*, vol. 137, pp. 205–215, 2017, DOI: https://doi.org/10.1016/j.polymdegradstab.2017.01.019

[11] F. Carpentier, S. Bourbigot, and M. Le Bras, “Rheological investigations in fire retardancy : application to ethylene – vinyl-acetate copolymer – magnesium hydroxide / zinc borate formulations,” *Polym. intrnational SCI*, vol. 1221, no. November 1999, 2000, DOI: https://doi.org/10.1002/1097-0126(200010)49:10<1216::AID-PI515>3.0.CO;2-S

[12] S. Bourbigot, J. Sarazin, F. Samyn, and M. Jimenez, “Intumescent ethylene-vinyl acetate copolymer : Reaction to fi re and mechanistic aspects,” *Polym. Degrad. Stab.*, vol. 161, pp. 235–244, 2019.

[13] D. L. Chung, “Review Graphite,” *J. Mater. Sci.*, vol. 7, pp. 1475–1489, 2002, DOI: https://doi.org/10.1023/A:1014915307738

[14] G. Camino, S. Duquesne, R. Delobel, B. E, C. Lindsay, and T. Roels, “Mechanism of Expandable Graphite Fire Retardant Action in Polyurethanes,” *ACS Symp. Ser.*, 2001, DOI: 10.1021/bk-2001-0797.ch008

[15] W. Focke, H. Badenhorst, W. Mhike, H. J. Kruger, and D. Lombaard, “Thermochimica Acta Characterization of commercial expandable graphite fire retardants,” *Thermochim. Acta*, vol. 584, pp. 8–16, 2014, DOI: http://dx.doi.org/10.1016/j.tca.2014.03.021

[16] G. Camino, A. Maffezzoli, M. Braglia, M. De Lazzaro, and M. Zammarano, “Effect of hydroxides and hydroxycarbonate structure on fire retardant effectiveness and mechanical properties in ethylene-vinyl acetate copolymer,” *Polym. Degrad. Stab.*, vol. 74, pp. 457–464, 2001, DOI: https://doi.org/10.1016/S0141-3910(01)00167-7

[17] E. Doctorale, “UNIVERSITÉ DES SCIENCES ET TECHNOLOGIE DE LILLE 1 Combination of mass loss cone, Fourier transform infrared spectroscopy and electrical low pressure impactor to extend fire behaviour characterization of materials,” 2014.

[18] Norme ISO 13927. Plastics-simple heat release test using a conical radiant heater and a thermopile detector. 2001.

[19] Norme ISO 5660-1. Reaction-to-fire tests - heat release, smoke production and mass loss rate. 2002.

[20] R. Filipczak, S. C. Ã, and R. E. Lyon, “Heat release rate measurements of thin samples in the OSU apparatus and the cone calorimeter,” Fire Saf. J., vol. 40, pp. 628–645, 2005, DOI: https://doi.org/10.1016/j.firesaf. 2005.05.009

[21] L. Gay, S. Bourbigot, and F. Ngohang, “Smoke composition using MLC / FTIR / ELPI: Application to fl ame retarded ethylene vinyl acetate,” *Polym. Degrad. Stab.*, vol. 115, pp. 89–109, 2015, DOI: https://doi.org/10.1016/j.polymdegradstab.2015.03.002

[22] S. E. Gustafsson and S. E. Gustafsson, “Transient plane source techniques for thermal conductivity and thermal diffusivity measurements of solid materials Transient diffusivity plane source techniques for thermal conductivity measurements of solid materials and thermal,” *Rev. Sci. instrumentscientific instruments*, vol. 797, no. 1991, 2000, DOI: https://doi.org/10.1063/1.1142087

[23] E. G. Gordeev, A. S. Galushko, and V. P. Ananikov, “Improvement of quality of 3D printed objects by elimination of microscopic structural defects in fused deposition modeling,” *journal.pone*, 2018, DOI: https://doi.org/10.1371/journal.pone.0198370

[24] Y. Li *et al.*, “Effect of Expandable Graphite Particle Size on the Flame Retardant, Mechanical, and Thermal Properties of Water-Blown Semi-Rigid Polyurethane Foam,” *J. Appl. Polym. Sci.*, 2013. DOI: https://doi.org/10.1002/app.39885

[25] J. Li, X. Mo, Y. Li, H. Zou, and M. Liang, “Influence of expandable graphite particle size between expandable graphite and ammonium,” *Polym. Bull.*, pp. 5287–5304, 2018, DOI: https://doi.org/10.1007/s00289-018-2309-y

[26] J. S. Reid *et al.*, “Stefan ’ s measurement of the thermal conductivity of air,” *Eur. J. Phys.*, vol. 5, 1984. DOI: https://doi.org/10.1088/0143-0807/5/1/003

Appendix

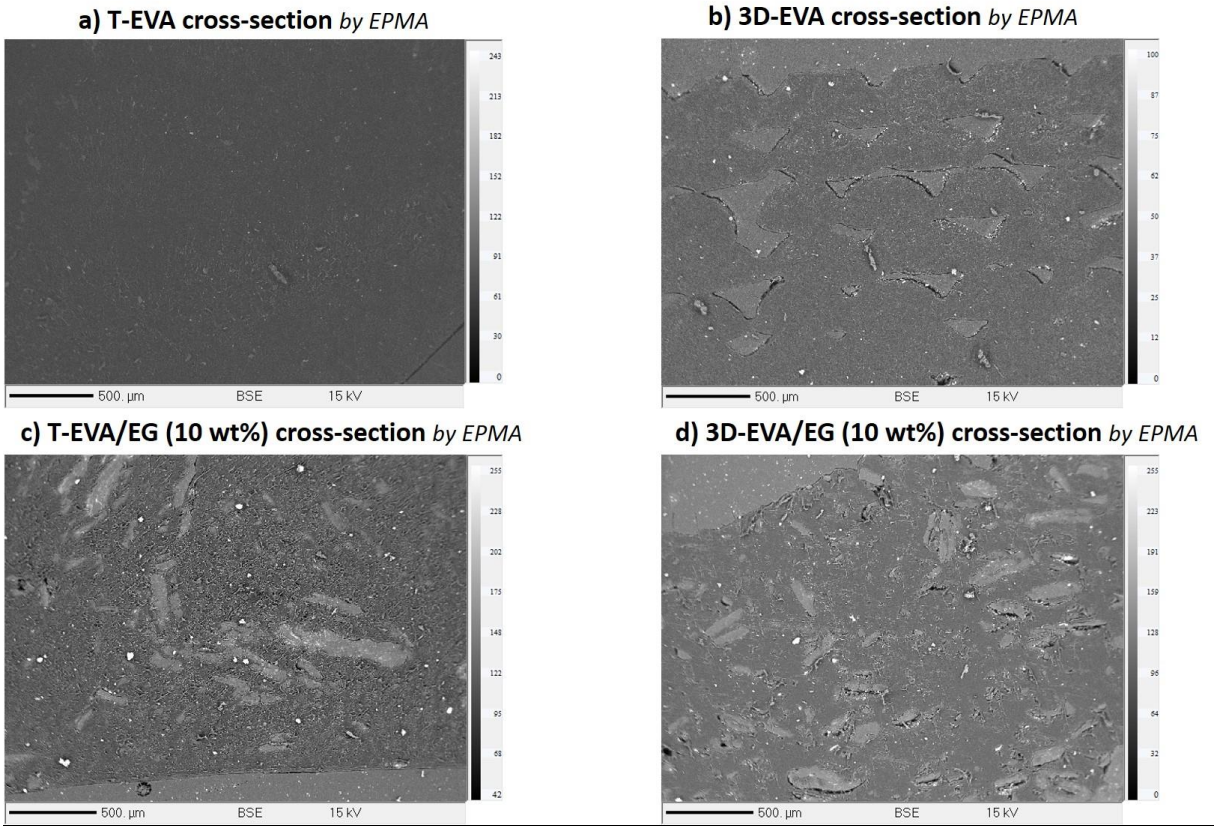

Figure A1. *EPMA cross-section observations (a)T-EVA, b) 3D-EVA, c) T-EVA/EG (10 wt%), d) 3D-EVA/EG (10 wt%))*

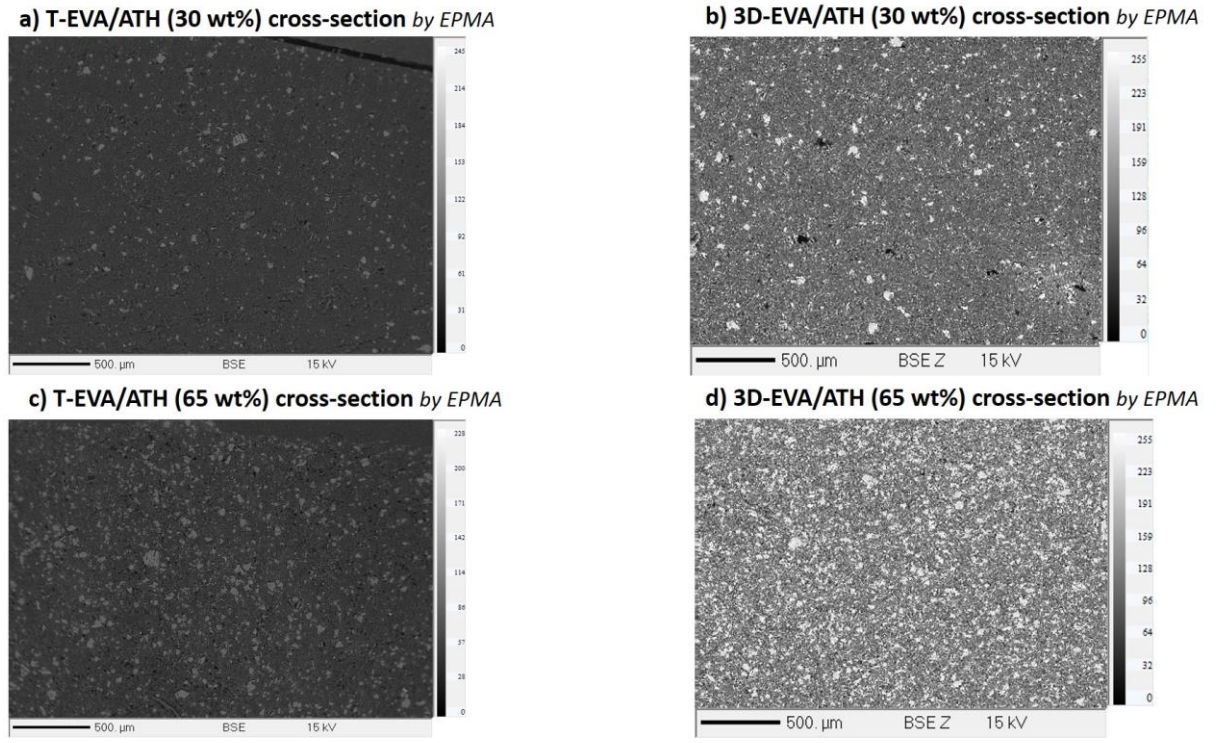

Figure A2. *EPMA cross-section observation (a) T-EVA/ATH (30 wt%), b) 3D-EVA/ATH (30 wt%), c) T-EVA/ATH (65 wt%), d) 3D-EVA/ATH (65 wt%))*